Supporting Information

Monecke et al. 10.1073/pnas.1215214110

SI Materials and Methods

Protein Expression and Purification. The cDNA of *Chaetomium thermophilum* chromosome region maintenance 1 (CRM1; *ct*CRM1; exportin1, XPO1) encoding the full-length protein (amino acids 1–1077) was cloned by using EcoRI and NotI restriction sites into a modified pET24d vector. The constructed GST-CRM1 fusion protein contains an interjacent tobacco etch virus (TEV) protease cleavable site and was expressed in *Escherichia coli* BL21(DE3) (Merck). Transformed cells were grown in kanamycin containing 2YT medium supplemented with 2% (wt/vol) α-D-glucose at 37 °C to an OD_{600} of 0.6. Temperature was set to 20 °C and protein expression was induced at an OD_{600} of 0.9 by adding IPTG to a final concentration of 0.6 mM. Cells were harvested after 20 h of induction (5,000 × *g*, 20 min, 4 °C) and resuspended in lysis buffer (500 mM NaCl, 50 mM Hepes/NaOH, pH 7.5, 2 mM $MgCl_2$, and 4 mM DTT). Cells were disrupted using a Microfluidizer 110S (Microfluidics), and the clarified lysate (30,000 × *g*, 30 min, 4 °C) was subsequently loaded onto a GSTrap column (GE Healthcare) equilibrated with lysis buffer. Unbound proteins were removed by washing with two column volumes of lysis buffer, and the bound fusion protein was eluted with a buffer containing additionally 30 mM reduced glutathione. For cleavage, the GST–[TEV]–CRM1 fusion protein was incubated with TEV protease (Invitrogen) at 4 °C overnight in a 1:100 molar ratio of protease:fusion protein. To remove remaining contamination with DNA and/or RNA, 5 μL Benzonase (Merck) was added to the solution. The TEV-cleaved protein was further purified by using a Superdex S200 (26/60) gel filtration column (GE Healthcare) in a buffer containing 150 mM NaCl, 20 mM Hepes/NaOH, pH 7.5, 2 mM $MgCl_2$, and 4 mM DTT. Fractions containing CRM1 were pooled and finally passed over another GSTrap to remove remaining traces of GST and uncleaved fusion protein. Highly pure *ct*CRM1 was concentrated to 20 mg/mL by using Millipore concentrators with a molecular weight cutoff of 30,000 Da (Merck), and 80-μL aliquots were frozen in liquid nitrogen and stored at −80 °C.

Crystallization and Crystal Structure Determination. Purified full-length *ct*CRM1 (amino acids 1–1077) was crystallized in a condition containing 22% (wt/vol) polyacrylic acid sodium salt 5100, 20 mM $MgCl_2$, 100 mM CHES/NaOH, pH 9.0, and 4% (vol/vol) 2,5 hexanediol. Rod-shaped orthorhombic crystals (typically 60 × 60 × 300 μm) grew at 20 °C after 15 d when mixing 1 μL of the reservoir and 1 μL of the protein solution (19 mg/mL). Crystals belong to space group $P2_12_12_1$ with cell dimensions as follows: a, 85.1 Å; b, 139.1 Å; and c, 174.9 Å. The crystals were flash-cooled in liquid nitrogen after soaking in reservoir solution containing, additionally, 14% (vol/vol) glycerol as cryoprotectant.

A diffraction data set has been collected at a wavelength of 0.9184 Å and a temperature of 100 K on BL14.1 operated by the Helmholtz-Zentrum Berlin at the BESSY II electron storage ring (Berlin-Adlershof, Germany) (1). The dataset was integrated and scaled by using iMOSFLM (2) and SCALA (3), respectively.

The structure was solved by means of molecular replacement with PHASER (4) by using the crystal structure of *Mus musculus* CRM1 as search model, which had been extracted from the CRM1–RanGTP–SPN1 complex [Protein Data Bank (PDB) ID code 3GJX] (5). The search was performed with two separate parts of mouse CRM1 (amino acids Ile130-Arg594 and Ala633-Ala1059), which were placed successively by the program. Mouse and *C. thermophilum* CRM1 share a sequence identity and similarity of 50% and 62%, respectively. The sequence was adjusted to *ct*CRM1 and the structure refined by iterative cycles of CNS (6) and manual model building in Coot (7) using a series of mFo-DFc simulated annealing electron density omit maps as implemented in CNS. The final round of refinement was performed with PHENIX (8). The model contains 1,067 of 1,077 residues and was refined at a resolution of 2.94 Å to R and R_{free} values of 22.03% and 24.28%, respectively (Table S1). The first two HEAT repeats were poorly defined in the initial 2mFo-DFc map and therefore have been entirely modeled based on simulated annealing omit maps. Model analysis by using MolProbity (9) revealed that there are 94.52% of the residues in the favored, 4.91% in the allowed, and 0.57% in the disallowed regions.

Trigonal crystals of *ct*CRM1 (amino acids 1–1077) grew in a condition containing 22% (wt/vol) polyacrylic acid sodium salt 5100, 20 mM $MgCl_2$, and 100 mM CHES/NaOH, pH 9.0, with a protein concentration of 13 mg/mL. Hexagonal-shaped crystals (typically 100 × 100 × 30 μm) grew at 20 °C after 5 d. Crystals belong to space group $P3_1$ with cell dimensions as follows: a, 89.8 Å; b, 89.8 Å; and c, 316.2 Å. Crystals were flash-cooled according to the protocol for orthorhombic *ct*CRM1, and a diffraction dataset has been collected on beam line P14 at the PETRA III electron storage ring (European Molecular Biology Laboratory, Hamburg, Germany) at a wavelength of 1.2395 Å and a temperature of 100 K. The dataset was integrated and scaled using XDS (10) and XSCALE, and the structure was solved by means of MR (PHASER) using two separate parts of the previously solved orthorhombic *ct*CRM1 structure (amino acids Pro2-Gln641 and Asn643-Lys1068). After careful inspection of the data, merohedral twinning was detected (twin law h,-h-k,-l; twin fraction, 0.46) and implemented in the PHENIX refinement. A gradient map as implemented in CNS for a model missing the acidic loop residues is shown in Fig. S4*B*. There are two CRM1 molecules in the asymmetric unit, and the structure was refined to R and R_{free} values of 21.61% and 23.56%, respectively. A total of 96.64% of the residues are located in the favored, 2.87% in the allowed, and 0.49% in the disallowed regions. All structure figures were generated using PyMOL (2002; DeLano Scientific).

EM Preparation and Image Processing. Purified *ct*CRM1 was stabilized using the GraFix protocol (11). The sample was loaded on a 5% to 20% (wt/vol) sucrose gradient in standard buffer containing 0% to 0.1% (vol/vol) glutaraldehyde and was centrifuged in a TH660 rotor (Sorvall) for 20 h at 40,000 rpm at 4 °C. Gradients were fractionated from the bottom, and fixing reaction was quenched by adding 25 mM glycine, pH 7.4. Complexes were then bound to a thin carbon film and transferred to an EM grid covered with a perforated carbon film. The bound molecules were stained with 2% (wt/vol) uranyl formate and air-dried. Images were recorded at a magnification of 155,000× on a 4k × 4k CCD camera (TVIPS) using twofold pixel binning (1.85 Å/pixel) in a CM200 FEG electron microscope (Philips/FEI) operated at 160 kV acceleration voltage (Fig. S8*B*).

A total of 34,000 particle images (144 × 144 pixels) were selected with the custom-written software johnhenry (manuscript in preparation). All valid particles were used to obtain the final result. None of the selected particles was excluded. A total of 13,017 particles were assigned to the compact conformation, and 20,952 particles were assigned to the extended conformation. Contrast transfer function correction was performed on the particle

images based on their classified power spectra (12). Further image processing was done in Imagic (13).

Contrast transfer function-corrected images were coarsened by a factor of two to a pixel size of 3.7 Å/pixel, and reference free-alignment was performed. After several rounds of exhaustive multireference alignment based on resampling in polar coordinates (14) and multivariate statistical analysis (15), stable class averages were obtained (Fig. S7 *A* and *B*). Starting models were generated by using angular reconstitution facilitated by a voting algorithm (16). The handedness was determined from the solved crystal structures. Two distinct conformations could be detected in the dataset, and it was split based in the cross correlation toward both models. To crosscheck those two models, angles for class averages from one model were determined using the other model (Fig. S8*A*). By iterating this procedure, models relaxed to their initial state. Models were further refined to yield a resolution of ~20 Å by projection matching. Resolution was judged by Fourier shell correlation using a cutoff of 0.5 (Fig. S7 *C* and *D*).

Molecular Dynamics Simulations. All simulations were carried out using Gromacs 4.5 (17, 18). The Amber99sb force field (19) was used together with the extended simple point charge water model (20). Electrostatic interactions were calculated using particle-mesh Ewald (21), with a real space cutoff of 1 nm, a grid spacing of 0.13 nm, and cubic interpolation. van der Waals interactions were cut off at a distance of 1.6 nm. Nonbonded interactions were calculated by using neighbor lists, which were updated every five time steps. All simulations were performed in the constant particle number, pressure, and temperature ensemble, using the velocity rescaling method for temperature coupling (22) with a heat bath temperature T of 300 K, a coupling time constant of 0.1 ps, and Berendsen pressure coupling (23), with a reference pressure of 1,000 hPa and a respective coupling time constant of 1 ps. All systems were simulated in dodecahedron-shaped simulation boxes using periodic boundary conditions. All bond lengths were constrained using the LINCS algorithm (24), meaning that harmonic pair bond interactions were removed from the force field potential and replaced by constraints. Additionally degrees of freedom representing fast fluctuations of angles defined by at least one hydrogen atom were removed by changing the respective hydrogen atoms into virtual sites and fixing the angle (25). The equations of motion were integrated using the Verlet algorithm (26) with a time step of 4 fs. Sodium chloride ions were added to ensure neutrality of the simulation box.

System Setup. Four simulation systems based on the extended conformation crystal structure of CRM1 (PDB ID code 4FGV) were constructed: a WT system, a system with a deleted C-terminal helix and the adjacent tail, a system with a deleted acidic loop, and a system containing both deletions. For the C-terminal deletion mutant, all residues starting at Glu1039 were removed. For the acidic loop deletion mutant, residues Glu419 to Asp446 were removed and replaced by a "GGSGGSG" motif, similar to that reported by Lee et al. (27), using Modeler 9v8 software (28).

Five and ten 100-ns unbiased simulations were performed for the WT and double deletion mutant, respectively. For the C-terminal deletion mutant, ten 200-ns simulations were carried out, and, for the acidic loop deletion mutant, five 100-ns simulations were performed.

Before all simulations, an energy minimization of the force field potential was performed by steepest descent, until the step size reached single point precision.

Data Analysis. To compare trajectories from the three different CRM1 structures [the CRM1–RanGTP–SPN1 complex (compact structure, PDB ID code 3GJX), the CRM1–SPN1 complex (almost compact structure, PDB ID code 3GB8), and free CRM1 (extended structure, PDB ID code 4FGV)], a common subset of C_α atoms was selected from residues that are identical in these three proteins. They were determined from a sequence alignment and restricted to the α-helical regions of the open conformation. This set of joint C_α atoms was used to define the linear vectors that connect the three crystal structures and the subsequent construction of the 2D plane in the configurational space that is defined by the three crystal structures. Furthermore, it was used as the subset for a principal component analysis (PCA) of the collected simulations of the mutant with the deleted C-terminal helix, as well as for the projections of the crystal structures and the simulated trajectories onto those vectors.

Nuclear Export Signal Cleft Analysis. For analysis of the behavior of the nuclear export signal (NES) cleft, it was defined to consist of the residues Glu507 to Met527 and Trp556 to Met570 of the extended structure. The C_α atoms of this subset, together with their corresponding counterparts in the compact and almost compact structure, were used to calculate the plane in configurational space defined by the NES cleft atoms of the three crystal structures. For each point in time in every trajectory, the NES cleft was defined to be closed if the Gaussian filtered projection onto the plane defined by the NES configurations in the three crystal structures was closer to the 4FGV structure than to the other structures. Similarly, for each time step, the overall conformation was assigned to an extended or compact ensemble. For this four-state model, the individual probabilities and conditional probabilities of the NES cleft being in the open conformation with the overall structure being extended or compact were calculated. The obtained probability p_i is assumed to be normally distributed with an SD of σ_i being equal to $p_i\,(1 - p_i) / n$, being the effective number of independent samples estimated from the autocorrelation time. A hypothesis test against the null hypothesis, i.e., $P\ (\mathrm{NES}_{\mathrm{open}} \mid \mathrm{CRM1}_{\mathrm{compact}}) = P\ (\mathrm{NES}_{\mathrm{open}} \mid \mathrm{CRM1}_{\mathrm{extended}})$ yields significances for these results of 2.3 and 2.6 SDs for the helix deletion and the double deletion mutant, respectively. To crosscheck the obtained probabilities and significances, the transition rates among the four states were estimated from the trajectories. Using these rates, artificial random trajectories were generated in a bootstrap-like approach. Mean and SD of the bootstrap distribution were then used to estimate the conditional probabilities and the corresponding errors. The approach yielded very similar although slightly different values and significances of 1.8 and 3.4 SDs.

1. Mueller U, et al. (2012) Facilities for macromolecular crystallography at the Helmholtz-Zentrum Berlin. *J Synchrotron Radiat* 19(pt 3):442–449.
2. Battye TGG, Kontogiannis L, Johnson O, Powell HR, Leslie AGW (2011) iMOSFLM: A new graphical interface for diffraction-image processing with MOSFLM. *Acta Crystallogr D Biol Crystallogr* 67(pt 4):271–281.
3. Collaborative Computational Project, Number 4 (1994) The CCP4 suite: Programs for protein crystallography. *Acta Crystallogr D Biol Crystallogr* 50(pt 5): 760–763.
4. McCoy AJ, et al. (2007) Phaser crystallographic software. *J Appl Cryst* 40(pt 4):658–674.
5. Monecke T, et al. (2009) Crystal structure of the nuclear export receptor CRM1 in complex with Snurportin1 and RanGTP. *Science* 324(5930):1087–1091.
6. Brünger AT, et al. (1998) Crystallography & NMR system: A new software suite for macromolecular structure determination. *Acta Crystallogr D Biol Crystallogr* 54(pt 5): 905–921.
7. Emsley P, Lohkamp B, Scott WG, Cowtan K (2010) Features and development of Coot. *Acta Crystallogr D Biol Crystallogr* 66(pt 4):486–501.
8. Adams PD, et al. (2010) PHENIX: A comprehensive Python-based system for macromolecular structure solution. *Acta Crystallogr D Biol Crystallogr* 66(pt 2): 213–221.
9. Chen VB, et al. (2010) MolProbity: All-atom structure validation for macromolecular crystallography. *Acta Crystallogr D Biol Crystallogr* 66(pt 1):12–21.
10. Kabsch W (2010) XDS. *Acta Crystallogr D Biol Crystallogr* 66(pt 2):125–132.

11. Kastner B, et al. (2008) GraFix: sample preparation for single-particle electron cryomicroscopy. *Nat Methods* 5(1):53–55.
12. Sander B, Golas MM, Stark H (2003) Automatic CTF correction for single particles based upon multivariate statistical analysis of individual power spectra. *J Struct Biol* 142(3):392–401.
13. van Heel M, Harauz G, Orlova EV, Schmidt R, Schatz M (1996) A new generation of the IMAGIC image processing system. *J Struct Biol* 116(1):17–24.
14. Sander B, Golas MM, Stark H (2003) Corrim-based alignment for improved speed in single-particle image processing. *J Struct Biol* 143(3):219–228.
15. van Heel M (1984) Multivariate statistical classification of noisy images (randomly oriented biological macromolecules). *Ultramicroscopy* 13(1-2):165–183.
16. Singer A, Coifman RR, Sigworth FJ, Chester DW, Shkolnisky Y (2010) Detecting consistent common lines in cryo-EM by voting. *J Struct Biol* 169(3):312–322.
17. Van Der Spoel D, Lindahl E, Hess B (2005) GROMACS: Fast, flexible, and free. *J Comput Chem* 26:1701–1718.
18. Hess B, Kutzner C, van der Spoel D, Lindahl E (2008) GROMACS 4: Algorithms for highly efficient, load-balanced, and scalable molecular simulation. *J Chem Theory Comput* 4:435–447.
19. Hornak V, et al. (2006) Comparison of multiple Amber force fields and development of improved protein backbone parameters. *Proteins* 65(3):712–725.
20. Berendsen HJC, Grigera JR, Straatsma TP (1987) The missing term in effective pair potentials. *J Phys Chem* 91:6269–6271.
21. Darden T, York D, Pedersen L (1993) Particle mesh Ewald: An N Log(N) method for Ewald sums in large systems. *J Chem Phys* 98:10089–10092.
22. Bussi G, Donadio D, Parrinello M (2007) Canonical sampling through velocity rescaling. *J Chem Phys* 126(1):014101–014101.
23. Berendsen HJC, Postma JPM, van Gunsteren WF, DiNola A, Haak JR (1983) Molecular dynamics with coupling to an external bath. *J Chem Phys* 81:3684–3684.
24. Hess B, Bekker H, Berendsen H, Fraaije J (1997) LINCS: A linear constraint solver for molecular simulations. *J Comput Chem* 18:1463–1472.
25. Feenstra K, Hess B, Berendsen H (1999) Improving efficiency of large time-scale molecular dynamics simulations of hydrogen-rich systems. *J Comput Chem* 20: 786–798.
26. Verlet L (1967) Computer "experiments" on classical fluids. I. Thermodynamical properties of Lennard-Jones molecules. *Phys Rev* 159:98–103.
27. Lee BJ, et al. (2006) Rules for nuclear localization sequence recognition by karyopherin beta 2. *Cell* 126(3):543–558.
28. Sali AA, Blundell TLT (1993) Comparative protein modelling by satisfaction of spatial restraints. *J Mol Biol* 234(3):779–815.

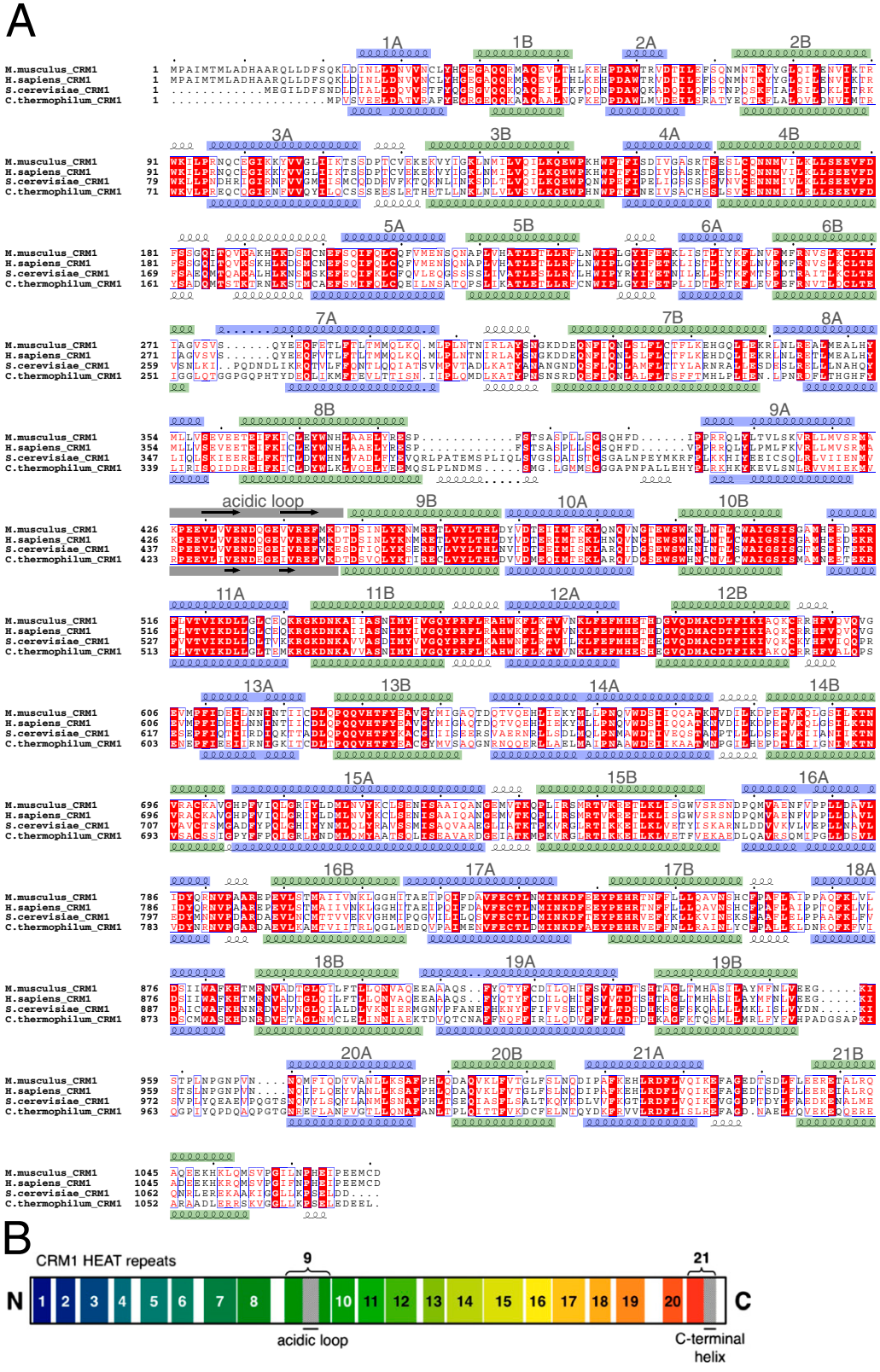

Fig. S1. Sequence alignment and schematic representation of *ct*CRM1. (*A*) Sequence alignment of mouse (*Mus musculus*), human (*Homo sapiens*), yeast (*Saccharomyces cerevisiae*) and *C. thermophilum* CRM1. Secondary structure elements are shown on top of the alignment for mouse CRM1 (PDB ID code 3GJX) and on the bottom for *ct*CRM1 (PDB ID code 4FGV). A-helices (blue) and B-helices (green) of the respective HEAT repeats align quite well and are labeled above the upper secondary structure assignment. *ct*CRM1 encompasses 1,077 aa and shows 62% sequence similarity (50% identity) to the human and 65% similarity (52% identity) to the yeast orthologue. (*B*) Schematic organization of HEAT repeats within *ct*CRM1. The HEAT repeats are numbered and colored from the N terminus (blue) to the C terminus (red). The acidic loop and the C-terminal helix are labeled.

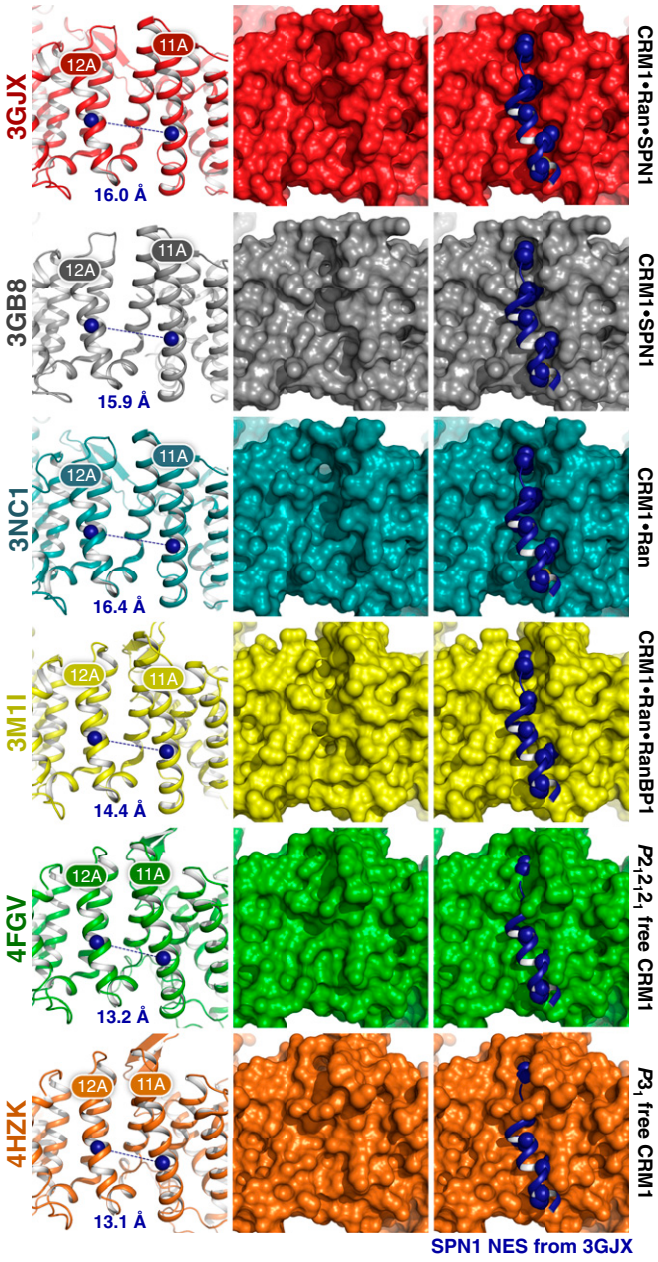

Fig. S2. Detail views of the NES cleft in different CRM1 crystal structures. A front view of the NES cleft is shown as a cartoon image (*Left*) with the centers of mass of the helices 11A and 12A represented by blue spheres. The distances between the centers of mass are denoted below. A surface model (*Middle*) illustrates the differences of the NES clefts between structures of CRM1 bound to SPN1 and RanGTP (PDB ID code 3GJX; red), CRM1 bound to SPN1 (PDB ID code 3GB8; gray), CRM1 bound to RanGTP (PDB ID code 3NC1; deep teal), CRM1 bound to RanGTP and RanBP1 (PDB ID code 3M1I; yellow) and free CRM1 in the orthorhombic (PDB ID code 4FGV; green) and the trigonal form (PDB ID code 4HZK; orange). A superposition of the individual models with the SPN1 NES from the ternary CRM1–RanGTP–SPN1 complex (*Right*) highlights the structural changes in the NES cleft, which are incompatible with NES binding in the free and RanBP1-bound CRM1 structures.

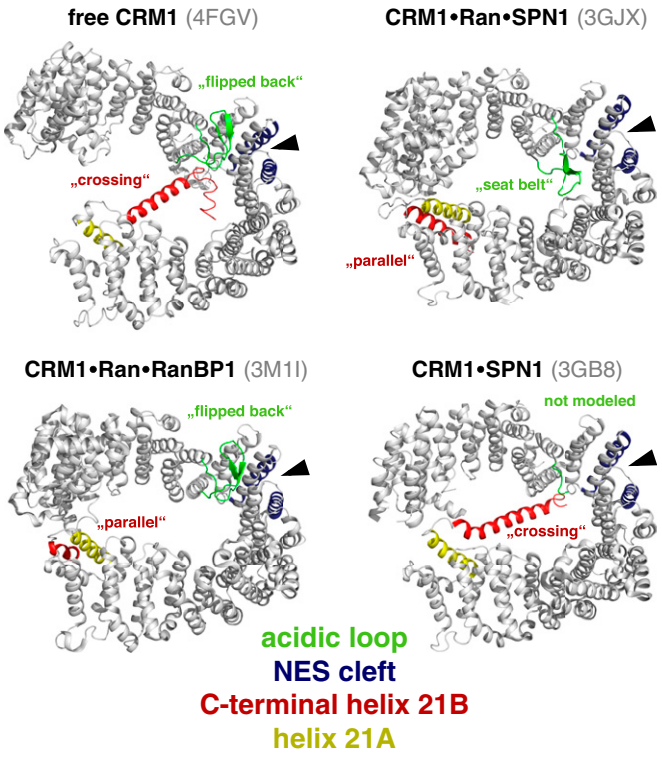

Fig. S3. Conformation and position of the acidic loop (green), the NES cleft (blue), helix 21A (yellow), and the C-terminal helix 21B (red) in different CRM1 crystal structures. For clarity reasons, only CRM1 is depicted in cartoon mode (light gray). Free CRM1 (*Upper Left*; PDB ID code 4FGV), CRM1–RanGTP–SPN1 (*Upper Right*; PDB ID code 3GJX), CRM1–RanGTP–RanBP1 (*Lower Left*; PDB ID code 3M1I), and CRM1–SPN1 (*Lower Right*; PDB ID code 3GB8) are shown. The acidic loop conformations are "flipped back" when bound to the back side of the NES cleft (black arrowhead), like in 4FGV and 3M1I; and in a "seatbelt" conformation when fixed by Ran and contacting the opposite side of CRM1 (like that of PDB ID code 3GJX). The conformation of the C-terminal helix is named "crossing" when it diagonally crosses the CRM1 arch and contacts a basic patch on the opposite side of CRM1 (like in PDB ID codes 3GB8 and 4FGV) and "parallel" when helix 21B is aligned in parallel to helix 21A (like in PDB ID codes 3GJX and 3M1I).

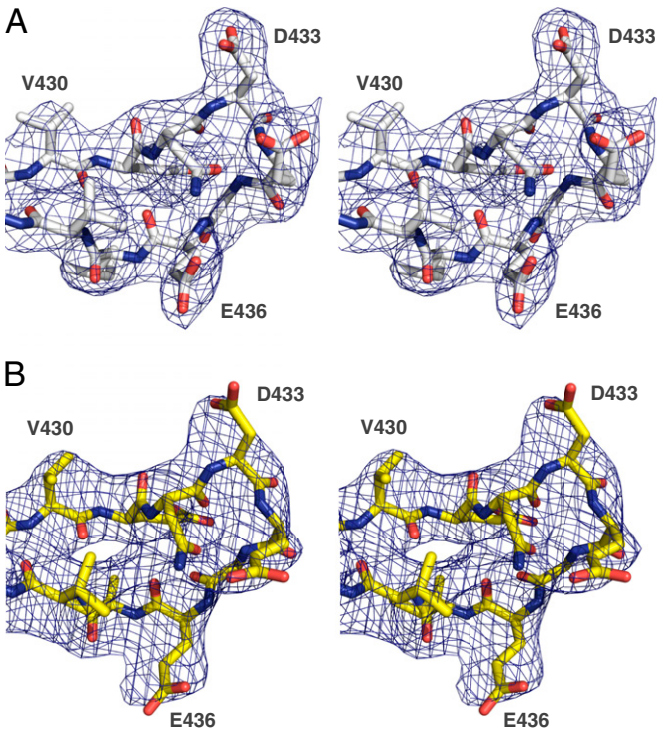

Fig. S4. Conformations and electron density omit maps of the acidic loop in free *ct*CRM1 crystal structures. (*A*) Stereo image of a representative mFo-DFc simulated annealing electron density omit map (residues 428–440 omitted) of the acidic loop from the orthorhombic crystal form (PDB ID code 4FGV). (*B*) For the trigonal crystal form, a stereo image of a representative electron density gradient map for a model lacking the acidic loop residues 428 to 440 was calculated as implemented in PHENIX (PDB ID code 4HZK). Stick models of the acidic loop residues are shown, and both electron density maps are contoured at a σ-level of 3.0.

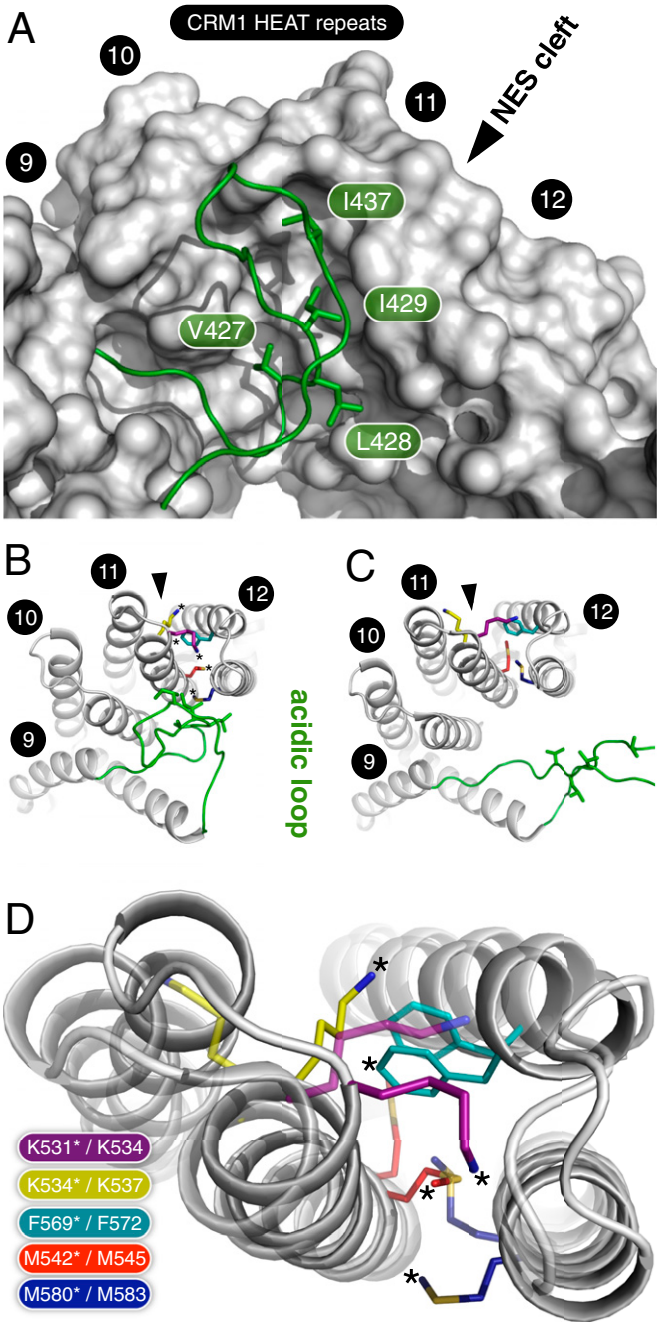

Fig. S5. Interactions of the acidic loop with the back side of the NES cleft stabilize its closed conformation. (*A*) Stabilization of the NES cleft in the closed conformation is achieved by hydrophobic interactions between residues of the acidic loop (green) and the area formed by the B-helices of HEAT repeats 11 and 12. HEAT repeats and residues of the acidic loop are labeled. Below the rearrangement of residues within the hydrophobic core of the helix bundle forming the NES cleft is shown for the extended conformation (PDB ID code 4FGV) (*B*) and the compact conformation (PDB ID code 3GJX) (*C*). The corresponding residues of the two structures are numbered and labeled in identical colors. (*D*) Superposition of only the prominent residues from *B* and *C* with the respective residues in identical colors. The rearrangements from the extended form (asterisk; PDB ID code 4FGV) to the compact conformation (transparent; PDB ID code 3GJX) are shown.

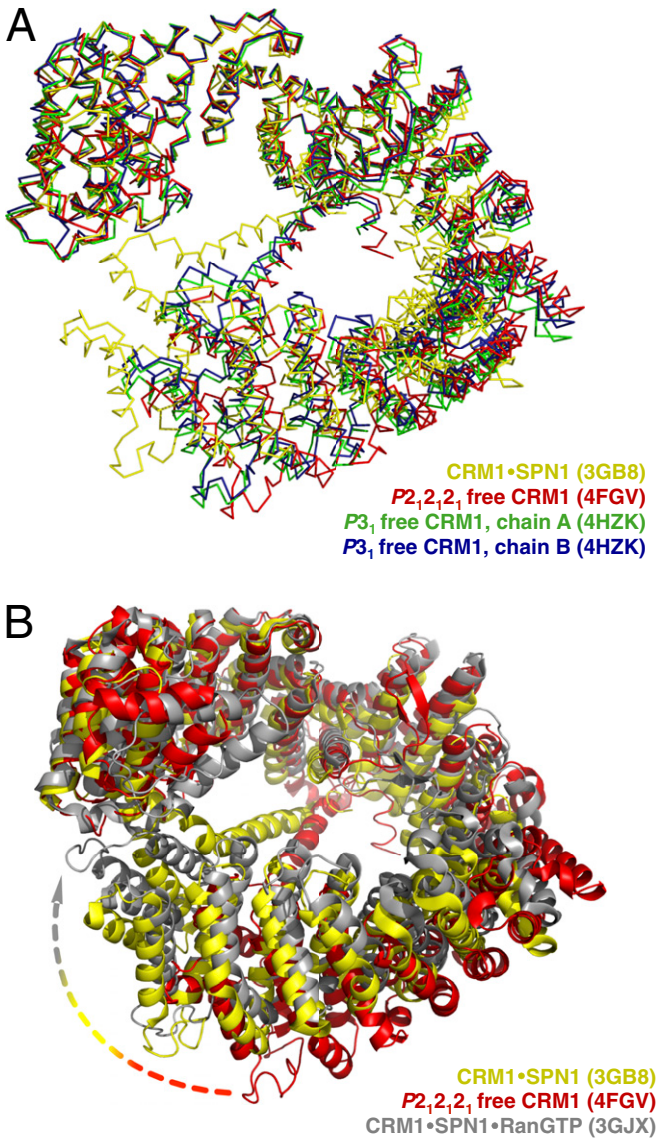

Fig. S6. Superposition of the two structures of free *ct*CRM1 ($P2_12_12_1$ and $P3_1$) and CRM1 bound to SPN1 (yellow) (*A*). For clarity reasons, only CRM1 is shown as C_α trace. Orthorhombic free CRM1 is shown in red, and the two molecules of the trigonal crystal form of free CRM1 are depicted in green and blue, respectively. Note the high degree of superposition of the free CRM1 structures in the N-terminal half of the molecule, restricting main structural changes to the C-terminal arch. (*B*) Superposition of free *ct*CRM1 (extended conformation, red), CRM1 bound to SPN1 (almost compact conformation, yellow), and CRM1 bound to RanGTP and SPN1 (compact conformation, gray).

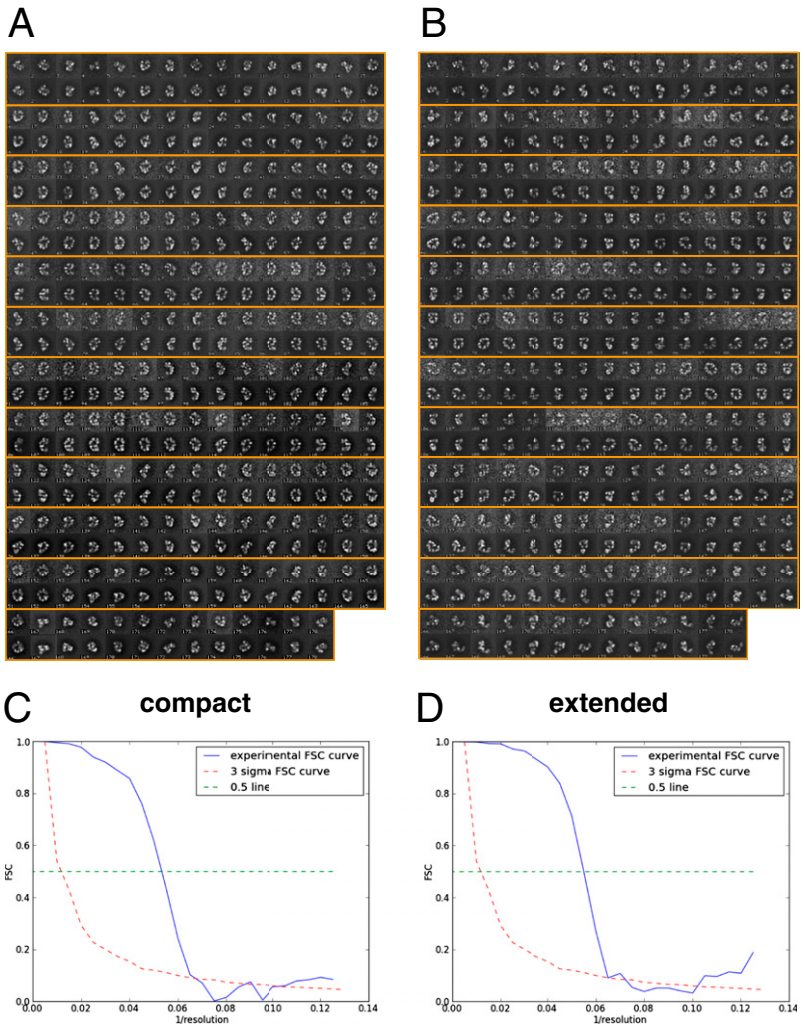

Fig. S7. EM data analysis. Reconstruction of the compact (*A*) and extended (*B*) conformation of *ct*CRM1. The particle classes 1 to 178 for each reconstruction are shown. Each orange framed row contains the particle sum (upper line) as well as the respective back projection (lower line) of a given particle class. Fourier shell correlation (FSC) curves for the compact (*C*) and extended (*D*) EM density maps were used to approximate the resolution of the respective models.

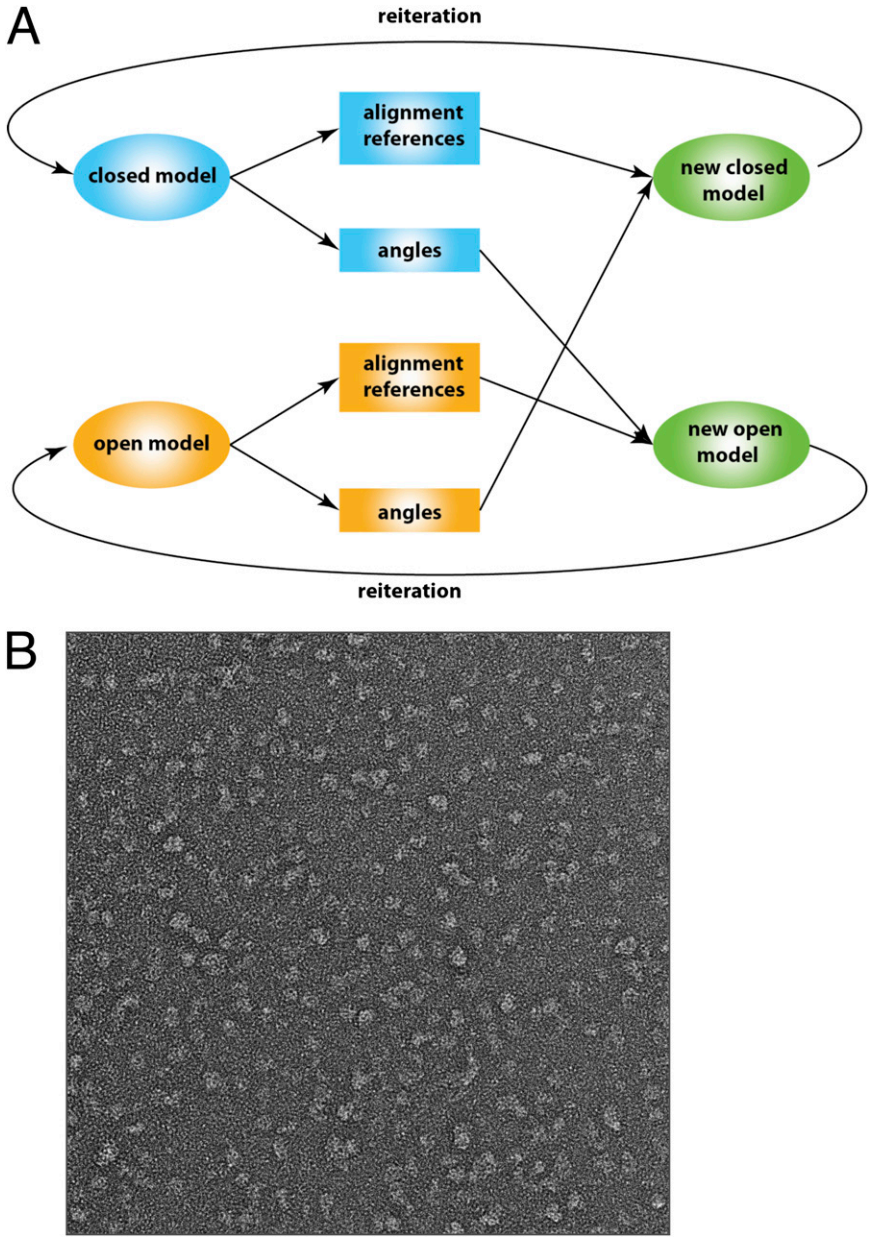

Fig. S8. Scheme for the EM data validation procedure used (*A*) and a representative EM raw image (*B*).

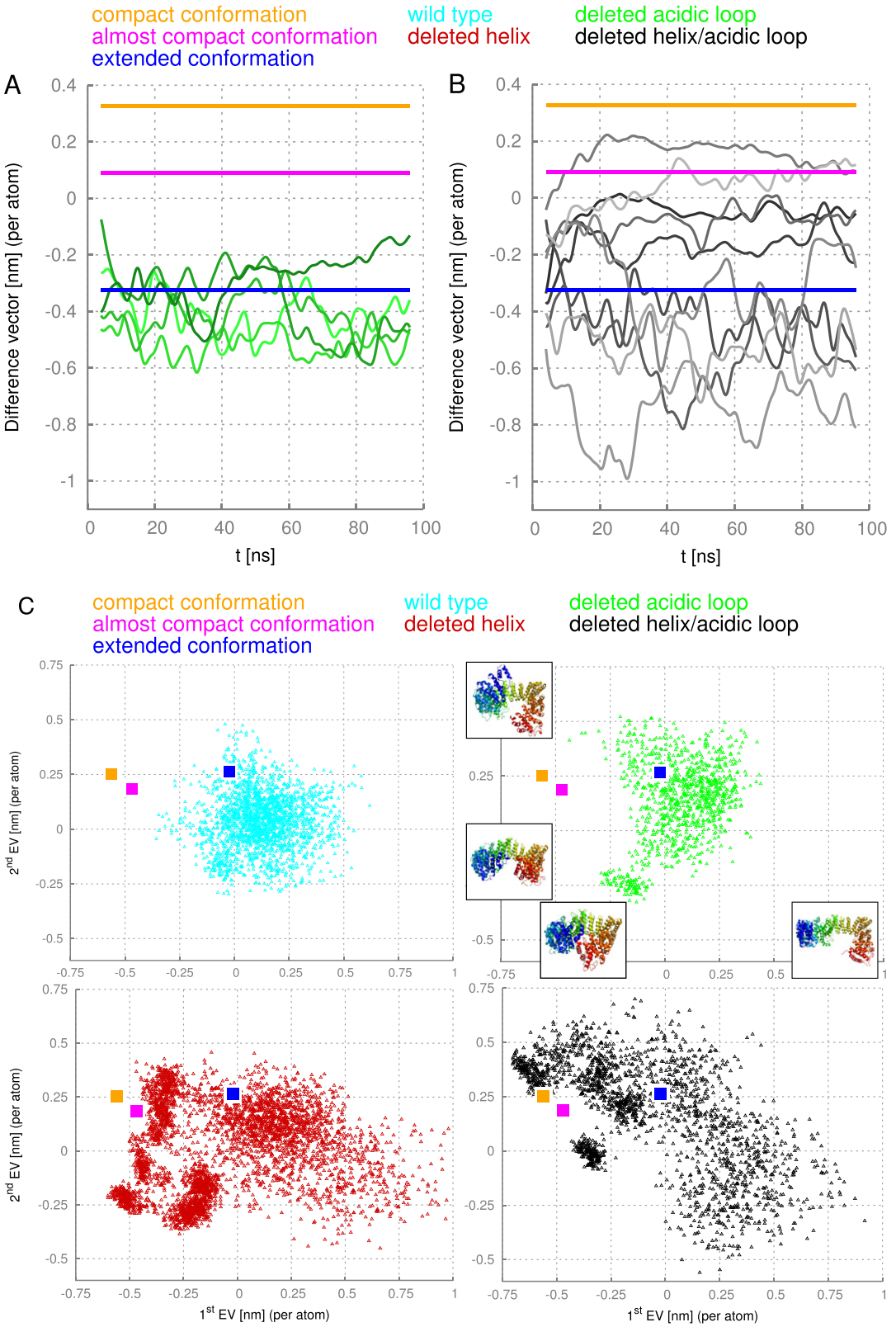

Fig. S9. Projections of the acidic loop deletion mutant (*A*, green) and the double deletion mutant (*B*, acidic loop and C-terminal helix deleted, gray) onto the difference vector between the extended (blue) and compact (orange) CRM1 structure. Note that deletion of the acidic loop alone does not change the structure significantly in molecular dynamics simulations. Additional deletion of the C-terminal helix increases the structural flexibility of the molecule and leads to a more compact conformation of CRM1. (*C*) Projections of WT and all mutant simulations onto the first two eigenvectors of a PCA of the helix deletion mutant simulation. The projections show dynamic movements during simulations along the second eigenvector that are not contained by the three crystal structures.

Table S1. X-ray data collection, refinement, and validation statistics for both crystal forms of full-length *C. thermophilum* CRM1

Variable	CRM1; BL14.1, BESSY II	CRM1; P14, PETRA III
Data collection		
Space group	$P2_12_12_1$	$P3_1$
Number of molecules/a.u.	1	2
Wavelength, Å	0.9184	1.2395
Cell dimensions		
a, *b*, *c;* Å	85.12, 139.07, 174.87	89.82, 89.82, 316.20
α, β, γ; °	90.00, 90.00, 90.00	90.00, 90.00, 120.00
Resolution, Å	51.44–2.94 (3.10–2.94)	50.00–3.10 (3.20–3.10)
R_{merge}	0.087 (0.545)	0.042 (0.562)
$I/\sigma(I)$	9.6 (2.1)	17.23 (2.18)
Completeness, %	96.4 (84.5)	96.9 (98.5)
Multiplicity	3.6 (3.3)	3.2 (3.2)
Refinement		
Resolution, Å	45.85–2.94	49.07–3.10
No. reflections	43,007	50,204
R_{work}	0.220	0.216
R_{free}	0.243	0.236
No. atoms	8,595	16,642
B-factors, Å^2	93.06	110.93/113.28 (chain A/B)
rmsd		
Bond lengths, Å	0.004	0.004
Bond angles, °	0.884	0.867
PDB ID code	4FGV	4HZK

All values in parentheses are for the respective highest resolution shell.

Table S2. Conditional probabilities of observing the NES cleft in the open conformation

Variable	Deleted helix 21B	Deleted acidic loop + helix 21B
P value		
NES_{open} vs. $CRM1_{extended}$	0.044 ± 0.021	0.070 ± 0.036
NES_{open} vs. $CRM1_{compact}$	0.121 ± 0.033	0.235 ± 0.060
Increase	0.023	0.010
Corresponding ΔΔG, kJ/mol	2.7 ± 1.4	3.5 ± 1.6

The probability of finding the NES cleft in an open conformation is increased by a factor of approximately three if CRM1 adopts the almost compact conformation compared with CRM1 in the extended conformation. This constitutes a significant shift in the free energy difference between the open and closed NES cleft conformation.

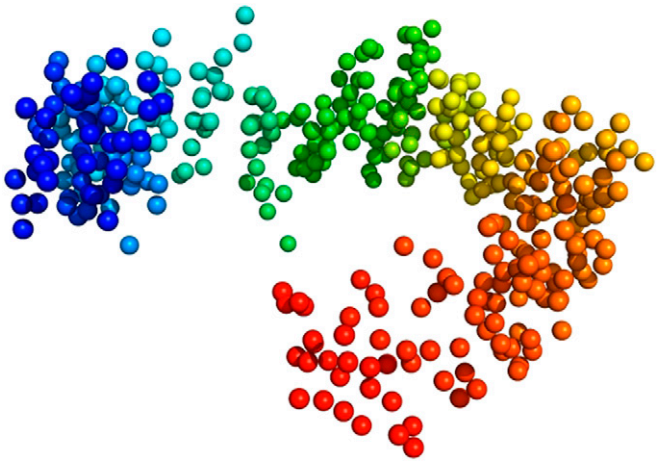

Movie S1. Main dynamics along eigenvector 1. Movements of *ct*CRM1 during the simulations along the first eigenvector of the PCA (Fig. S9*C*) constitutes solely a change in the diameter of the ring. The spheres represent a common subset of C_α atoms selected from residues that are identical in human, mouse, and *C. thermophilum* CRM1. Methodological details are provided in *SI Materials and Methods*.

Movie S1

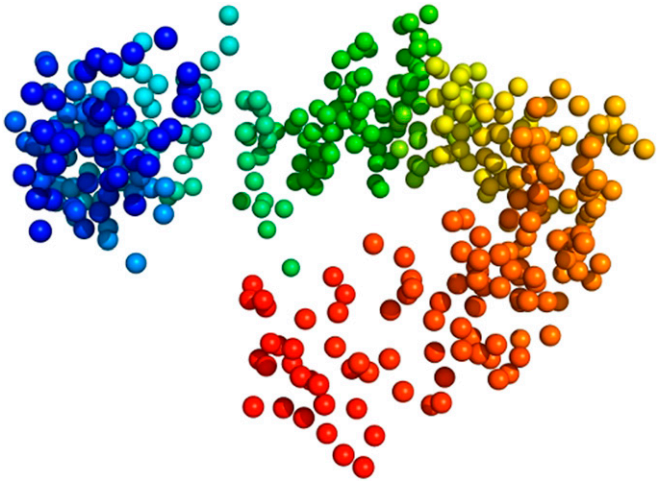

Movie S2. Main dynamics along eigenvector 2. Movements of *ct*CRM1 during the simulations along the second eigenvector of the PCA (Fig. S9*C*) constitutes solely a change in the pitch of the superhelix. The spheres represent a common subset of C_α atoms selected from residues that are identical in human, mouse, and *C. thermophilum* CRM1. Methodological details are provided in *SI Materials and Methods*.

Movie S2